fluids

MDPI

Article

Modeling and Hydrodynamic Simulation Analysis of an Underwater Jacket Cleaning Robot

Wenxing Sun [1], Duanjiao Li [1], Junwen Yao [2], Yun Chen [2], Yanjun Ma [2], Yongfei Ma [3,4], Xutao Chen [3,4] and Yupeng Zou [3,4,*]

[1] Guangdong Power Grid Co., Ltd., Guangzhou 510030, China; sunwenxing@dky.gd.csg.cn (W.S.); liduanjiao@gd.csg.cn (D.L.)
[2] Electric Power Research Institute of Guangdong Power Grid Co., Ltd., Guangzhou 510030, China; yaojunwen@gd.csg.cn (J.Y.); chenyun@gd.csg.cn (Y.C.); mayanjun@gd.csg.cn (Y.M.)
[3] Shandong Key Laboratory of Design and Manufacturing for High-End Offshore Oil and Gas Equipment, College of Mechanical and Electronic Engineering, China University of Petroleum (East China), Qingdao 266580, China; z25040097@s.upc.edu.cn (Y.M.); s25040054@s.upc.edu.cn (X.C.)
[4] Engineering Research Center of the Ministry of Education for New Equipment and Technology in Petroleum and Petrochemical Industry, China University of Petroleum (East China), Qingdao 266580, China
* Correspondence: zouyupeng@upc.edu.cn

Abstract

To address the cleaning requirements for marine growth on offshore platform jackets, an underwater cleaning robot featuring a combined "chassis + thruster-assisted adhesion + magnetic adhesion" mode is designed. The robot is equipped with four thrusters and a magnetic-adhesion wheeled chassis, enabling stable attachment and movement on varying-diameter pipes. Kinematic models in both inertial and body-fixed coordinate systems are established, and six-degree-of-freedom (6-DOF) dynamic equations are derived. These equations systematically incorporate key factors including added-mass forces, damping forces, hydrostatic restoring forces, ocean current disturbances, and thruster torques. Based on CFD simulations employing overset grids, moving reference frames, and simple harmonic motion techniques, the damping, added-mass, and thruster thrust and torque coefficients for each degree of freedom are identified. The obtained parameters demonstrate reasonable consistency with the CFD internal validation and preliminary external verification, providing a complete theoretical model and simulation data to support the motion control and operational stability analysis of the underwater cleaning robot. The established dynamic model addresses the free-navigation condition of the robot without cleaning operation. The additional hydrodynamic effects during cleaning operations will be considered in future work.

Keywords: underwater jacket cleaning robot; dynamic modeling; hydrodynamic coefficients; CFD simulation; propeller thrust

Check for updates

Academic Editor: Michel Benoit

Received: 11 June 2026
Revised: 10 July 2026
Accepted: 15 July 2026
Published: 18 July 2026

Copyright: © 2026 by the authors. Licensee MDPI, Basel, Switzerland. This article is an open access article distributed under the terms and conditions of the Creative Commons Attribution (CC BY) license.

1. Introduction

In current offshore oil exploitation, jacket structures serve as essential supporting components for platforms. Due to long-term immersion in the marine environment, their surfaces are highly susceptible to attachment by marine organisms such as barnacles, oysters, mussels, algae, and microbial biofilms, forming a marine biofouling layer with distinct spatiotemporal variations [1,2]. Marine biofouling increases the equivalent diameter, added mass, and surface roughness of structural components, alters flow separation and vortex-induced response characteristics, and consequently elevates drag forces, inertia forces, and

fatigue loads under wave and current actions [3–5]. Simultaneously, biofilms and their metabolites can induce or accelerate the microbiologically influenced corrosion (MIC) of metallic materials, diminishing the long-term effectiveness of protective coatings on marine steel structures [6–8]. With the rapid expansion of the marine economy and deep-sea oil and gas exploitation in the 21st century, drilling and production platforms have become core equipment in modern ocean development, making their maintenance and support increasingly critical. To ensure an adequate service life for jacket structures and guarantee the sustained stability of oil production, periodic cleaning and inspection are imperative. Currently, jacket cleaning still heavily relies on divers or remotely operated vehicles (ROVs) equipped with high-pressure water jet equipment. However, the underwater environment is complex and volatile; operations are easily disrupted by factors such as sea states, water depth, visibility, currents, and recoil forces, which limit cleaning efficiency and pose high safety risks to personnel [9]. Therefore, developing a specialized underwater climbing cleaning robot system tailored to jacket cleaning demands holds profound practical significance for enhancing the maintenance capability and operational safety of offshore oil production equipment [10,11].

In application scenarios such as underwater steel structure cleaning, climbing robots have advanced rapidly in recent years, owing to their advantages of ease of operation, robust environmental adaptability, and high operational stability. Focusing on underwater wall-climbing cleaning robots, research teams globally have conducted extensive investigations into adsorption methods, curvature adaptation, cleaning mechanisms, and path tracking. Wang et al. designed a hybrid wheel-leg robot with variable curvature for hull cleaning, which enhances conformable and stable adsorption on curved hulls via a permanent magnet wheel-leg mechanism [12]; Jiang et al. proposed a passive adaptive wall-climbing robot based on a five-bar mechanism, offering a structural design paradigm for stable locomotion on metallic walls with changing curvatures [13]; Aiming at marine cylindrical steel structures, Luo et al. presented a passive adaptive cleaning and inspection robot featuring tapered magnetic adhesion wheels, validating its locomotive capability on cylindrical surfaces of varying diameters through instability modeling and prototype testing [10]. Regarding cleaning execution and control, Chen et al. developed an underwater hull cleaning robot driven by thrusters and tracks, improving cleaning continuity via coverage path-tracking control [11]; Wei et al. proposed an underwater hull cleaning robot combining mechanical brushing and cavitation jetting to balance high-efficiency cleaning with surface damage control [14]; Zhong et al. verified the feasibility of using ultrasound-enhanced submerged cavitation jets for biofouling removal on ships [15]; and Zhu et al. further investigated the cavitation cleaning mechanism of barnacle fouling subjected to high-speed water jets [16].

The underwater jacket is composed of steel tubular members with various specifications and has a relatively special structural configuration. Therefore, the cleaning robot must not only adapt to non-uniform tubular diameters and curvature variations in vertical members, inclined braces, and joint regions, but also maintain stable adhesion and reliable crawling under the effects of ocean currents, waves, and near-wall flow interactions. Recent studies have shown that near-wall hydrodynamic interactions between underwater cleaning robots and large ship hulls or marine structures can significantly affect resistance, lateral forces, and flow-field distributions [17]. In addition, the surface roughness caused by marine biofouling can alter the maneuvering stability and near-bottom motion characteristics of underwater vehicles [18]. Therefore, the design of the cleaning robot should focus on its adhesion, locomotion, and disturbance-resistance capabilities under non-uniform tubular-diameter conditions. Meanwhile, the parameters of water-jet or cavitation-jet cleaning should be reasonably selected to balance cleaning efficiency, coating protection, and

structural safety [19,20]. To ensure that the cleaning equipment can be stably carried by the robot and that reliable crawling and cleaning operations can be achieved on the surface of the underwater jacket, systematic design and modeling analyses of the robot are carried out in this study.

2. Design Scheme of the Jacket Cleaning Robot

To achieve effective cleaning of underwater jacket structures, the design of the robot is primarily centered on the following three core functional requirements:

(1) Brushing and Cleaning Function: The ultimate operational objective of the robot is to remove marine organisms—such as barnacles, algae, and shellfish—adhering to the jacket surface. Given the high diversity and robust adhesion forces of these biofouling species, the cleaning mechanism must possess exceptional underwater adaptability and sufficient driving power. Furthermore, it should operate smoothly during brushing to minimize dynamic disturbances to the robot's locomotion posture, thereby ensuring the overall stability of the cleaning operation.

(2) Adhesion Function: The walls of offshore jacket structures are fabricated from steel materials featuring excellent magnetic permeability. However, due to the heavy accumulation of marine growth, the actual surface exhibits a highly irregular and rugged topography. Consequently, the robot must adopt a secure and reliable adhesion method that guarantees both flexible mobility and the absolute prevention of detachment during operation, thereby achieving stable and resilient attachment.

(3) Climbing and Locomotion Function: Jacket structures consist of vertical legs, horizontal braces, and diagonal braces. Legs have the largest diameter, and diagonal braces the smallest; all submerged components are highly prone to biofouling. The target surfaces present pronounced curvature variations and conspicuous obstacles; therefore, the robot's locomotion mechanism must exhibit robust geometric adaptability and reliable obstacle-negotiation performance.

To address the difficulty of conventional underwater cleaning robots in adapting to tubular members with different diameters and their unstable cleaning performance, this study analyzes the structures and functions of underwater climbing cleaning robots developed by domestic and international research institutions. Meeting all technical requirements and considering the operating environment of underwater cleaning tasks, a cleaning robot scheme combining a wheeled chassis, thruster-assisted adhesion, and magnetic adhesion is adopted. The robot adheres to the surface of the offshore jacket through the thrust generated by vertically mounted thrusters and the magnetic adhesion force provided by magnetic adhesion drive wheels. It moves along the jacket surface driven by the magnetic adhesion drive wheels, while the cleaning discs mounted on the robot perform the cleaning operation. The robot mainly consists of a magnetic adhesion wheeled chassis, cleaning discs, thruster assemblies, and a control compartment. The total mass of the robot is approximately m = 150 kg, and its principal inertia tensor is $I = \mathrm{diag}\{61.26, 54.63, 96.83\}$ kg·m^2. The overall dimensions are approximately L × W × H = 1.3 m × 1.2 m × 0.4 m. The simplified virtual prototype model and the detailed dimensional drawing are shown in Figures 1 and 2, respectively. The left and right horizontal thrusters are denoted as HP1 and HP2, respectively; the left and right vertical thrusters are denoted as VP1 and VP2, respectively; the left and right front wheels are denoted as FW1 and FW2, respectively; and the left and right rear wheels are denoted as BW1 and BW2, respectively.

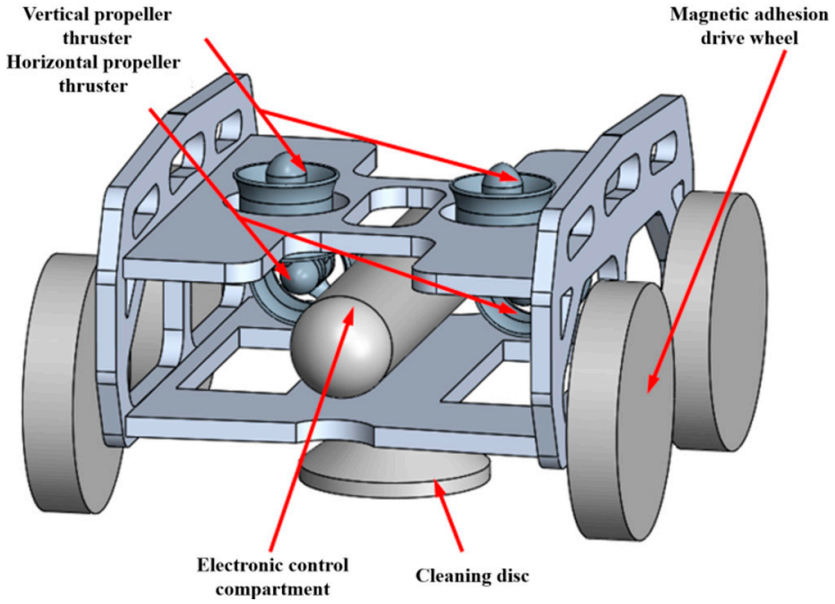


Figure 1. Simplified virtual prototype model of the underwater cleaning robot.

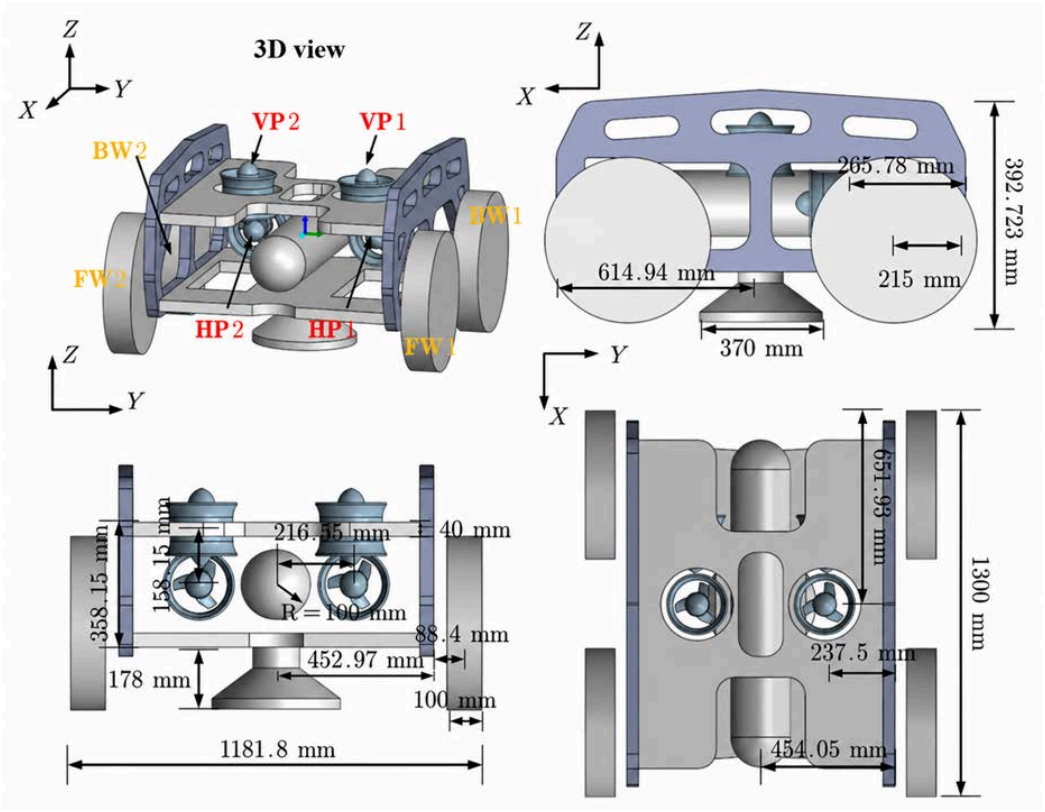


Figure 2. Dimensional drawing of the underwater cleaning robot.

Four T200 propeller thrusters with forward-rotation propellers are used to provide horizontal thrust and vertical thrust, the latter serving as the adhesion force. The relationship between propeller type and thrust is shown in Figure 3. The wheel diameter and width of the wheeled chassis are 0.5 m and 0.1 m, respectively. The positions of the thrusters and drive wheels relative to the robot's center of gravity are listed in Table 1.

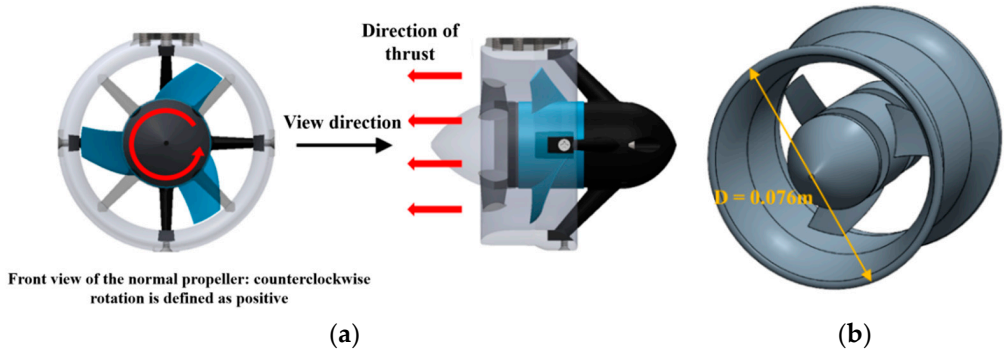


Figure 3. Thruster Model. (**a**) 3D model of the T200 thruster with a forward-rotation propeller. (**b**) Simplified model.

Table 1. Coordinates of the rotating-domain center with respect to the robot center of gravity.

	Propeller Thruster Center Coordinates (mm)				Wheel Center Coordinates (mm)			
Coordinate Values	**HP1**	**HP2**	**VP1**	**VP2**	**FW1**	**FW2**	**BW1**	**BW2**
X	2.86	2.86	−221.12	−221.12	400.93	400.93	−399.07	−399.07
Y	215	−215	222.5	−222.5	540.9	−540.9	540.9	−540.9
Z	129.91	129.91	−28.23	−28.23	−139.07	−139.07	−139.07	−139.07

3. Theoretical Modeling of the Offshore Jacket Cleaning Robot

3.1. Kinematic Modeling Analysis

3.1.1. Coordinate Systems and Kinematic Variables

To facilitate the mathematical description of the kinematic state variables of the underwater cleaning robot and the establishment of its dynamic model, an inertial frame $o_g x_g y_g z_g$, denoted as $\{g\}$, and a body-fixed frame $o_b x_b y_b z_b$, denoted as $\{b\}$, are defined. The inertial frame $\{g\}$ is fixed to the Earth. Since the curvature and rotation of the Earth are neglected, the Earth-fixed frame can be regarded as an inertial frame. The $o_g x_g$- and $o_g y_g$-axes lie in the horizontal plane, while the $o_g z_g$-axis is aligned with the direction of gravity. The origin of the body-fixed frame $\{b\}$ is fixed at the center of gravity of the underwater cleaning robot. The $o_b x_b$-axis and $o_b y_b$-axis point along the longitudinal and lateral directions of the robot, respectively, and the $o_b z_b$-axis points toward the ventral side of the robot. The unit vectors along the x-, y-, and z-axes are denoted by $\mathbf{e}_1$, $\mathbf{e}_2$, and $\mathbf{e}_3$, respectively. Both coordinate frames are right-handed. For the underwater cleaning robot, the center of buoyancy does not coincide with the center of gravity, while both are located on the $o_b z_b$-axis. The position vector from the origin o_b of the body-fixed frame to the center of gravity (CG) is defined as $\mathbf{r}_G = [x_G, y_G, z_G]^T = [0, 0, 0]^T$. The position vector from the origin o_b of the body-fixed frame to the center of buoyancy (CB) is defined as $\mathbf{r}_B = [x_B, y_B, z_B]^T = [0, 0, -0.1]^T$. The coordinate systems of the underwater cleaning robot are shown in Figure 4.

The position and attitude of the underwater cleaning robot, represented by Euler angles, are described in the inertial frame, whereas its linear and angular velocities are described in the body-fixed frame attached to the robot. According to the variable definitions specified by SNAME [21], the corresponding variables are listed in Table 2.

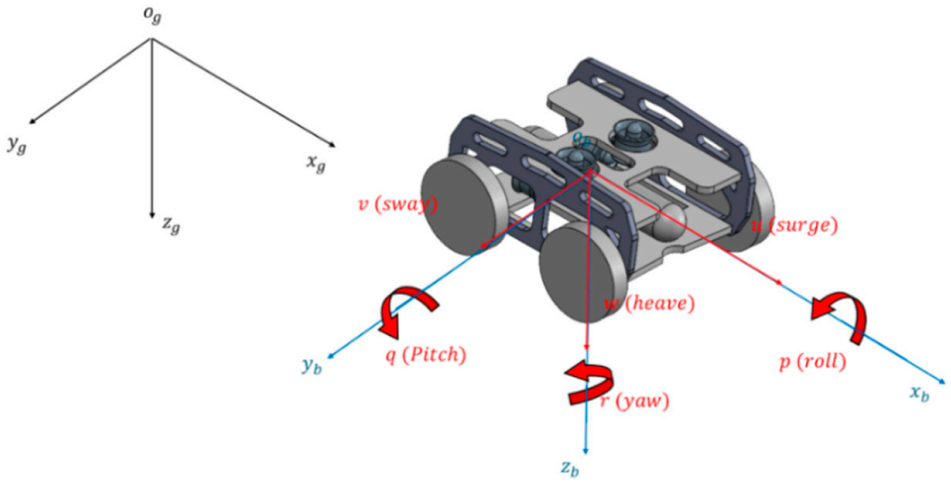


Figure 4. Coordinate systems of the underwater cleaning robot.

Table 2. Motion variable definitions for the underwater cleaning robot.

No.	DOF	Position and Euler Angles	Linear and Angular Velocities	Forces and Moments
1	Surge: translation along the X-axis	x	u	X
2	Sway: translational along the Y-axis	y	v	Y
3	Heave: translation along the Z-axis	z	w	Z
4	Roll: rotation about the X-axis	ϕ	p	K
5	Pitch: rotation about the Y-axis	θ	q	M
6	Yaw: rotation about the Z-axis	ψ	r	N

The six-degree-of-freedom motion and forces acting on the underwater cleaning robot are expressed in vector form as follows:

$$\begin{aligned} \boldsymbol{\eta} &= \left[\boldsymbol{\eta}_1^T, \boldsymbol{\eta}_2^T\right]^T; \boldsymbol{\eta}_1 = [x, y, z]^T; \boldsymbol{\eta}_2 = [\phi, \theta, \psi]^T; \\ \boldsymbol{\nu} &= \left[\boldsymbol{\nu}_1^T, \boldsymbol{\nu}_2^T\right]^T; \boldsymbol{\nu}_1 = [u, v, w]^T; \boldsymbol{\nu}_2 = [p, q, r]^T; \\ \boldsymbol{\tau} &= \left[\boldsymbol{\tau}_1^T, \boldsymbol{\tau}_2^T\right]^T; \boldsymbol{\tau}_1 = [X, Y, Z]^T; \boldsymbol{\tau}_2 = [K, M, N]^T \end{aligned} \tag{1}$$

where $\boldsymbol{\eta}$ denotes the position and attitude vector in the inertial frame, $\boldsymbol{\nu}$ denotes the linear and angular velocity vector in the body-fixed frame, and $\boldsymbol{\tau}$ denotes the vector of forces and moments acting on the underwater cleaning robot in the body-fixed frame. In addition, based on the force characteristics and motion state of the underwater cleaning robot, the following assumptions are made to facilitate the analysis of its motion:

Considering the complex positional relationship among the center of buoyancy, center of gravity, and center of mass of the underwater cleaning robot, the mass distribution of the robot is assumed to be uniform to simplify the analysis. Therefore, the coordinate system origin is set at the center of mass (coincident with the center of gravity under uniform gravity).

The symbols $\dot{\boldsymbol{a}}$ and $\widetilde{\boldsymbol{a}}$ are defined as the time derivatives of the vector $\boldsymbol{a}$ with respect to time in the inertial frame $\{g\}$ and the body-fixed frame $\{b\}$, respectively.

For the cross product of two (3×1) vectors $\mathbf{a} = [a_1, a_2, a_3]^T$ and $\mathbf{b} = [b_1, b_2, b_3]^T$, the skew-symmetric matrix $\boldsymbol{S}(\boldsymbol{a})$ is introduced such that $\boldsymbol{a} \times \boldsymbol{b} = \boldsymbol{S}(\boldsymbol{a})\boldsymbol{b}$ where:

$$\boldsymbol{S}(\boldsymbol{a}) = \begin{bmatrix} 0 & -a_3 & a_2 \\ a_3 & 0 & -a_1 \\ -a_2 & a_1 & 0 \end{bmatrix} \tag{2}$$

$\|\boldsymbol{a}\|$ denotes the Euclidean norm of the vector $\boldsymbol{a} = [a_1, a_2, ..., a_n]^T$, which is given by $\|\mathbf{a}\| = \sqrt{a_1^2 + a_2^2 + \ldots + a_n^2}$.

3.1.2. Kinematic Description

The kinematic relationship between the linear and angular velocities in the body-fixed frame and the velocity and attitude-rate variables in the inertial frame is established. Its vector form can be expressed as follows [22]:

$$\begin{bmatrix} \dot{\boldsymbol{\eta}}_1 \\ \dot{\boldsymbol{\eta}}_2 \end{bmatrix} = \underbrace{\begin{bmatrix} \boldsymbol{J}_1(\boldsymbol{\eta}_2) & \mathbf{0}_{3\times3} \\ \mathbf{0}_{3\times3} & \boldsymbol{J}_2(\boldsymbol{\eta}_2) \end{bmatrix}}_{J(\eta)} \begin{bmatrix} \boldsymbol{\nu}_1 \\ \boldsymbol{\nu}_2 \end{bmatrix} \Leftrightarrow \dot{\boldsymbol{\eta}} = \boldsymbol{J}(\boldsymbol{\eta})\boldsymbol{\nu} \tag{3}$$

where $\boldsymbol{J}(\boldsymbol{\eta})$ is the transformation matrix parameterized by the Euler angles, namely the roll angle ϕ, pitch angle θ, and yaw angle ψ, and is given by:

$$\boldsymbol{J}_1(\boldsymbol{\eta}_2) = \begin{bmatrix} c\theta c\psi & s\phi s\theta c\psi - c\phi s\psi & c\phi s\theta c\psi + s\phi s\psi \\ c\theta s\psi & s\phi s\theta s\psi + c\phi c\psi & c\phi s\theta s\psi - s\phi c\psi \\ -s\theta & s\phi c\theta & c\phi c\theta \end{bmatrix} \tag{4}$$

$$\boldsymbol{J}_2(\boldsymbol{\eta}_2) = \begin{bmatrix} 1 & s\phi t\theta & c\phi t\theta \\ 0 & c\phi & -s\phi \\ 0 & s\phi/c\theta & c\phi/c\theta \end{bmatrix} \tag{5}$$

where $\mathrm{s}\cdot = \sin(\cdot)$, $\mathrm{c}\cdot = \cos(\cdot)$, $\mathrm{t}\cdot = \tan(\cdot)$.

3.2. Dynamic Modeling Analysis

3.2.1. Rigid-Body Dynamic Analysis

The six-degree-of-freedom rigid-body equations of motion of the underwater cleaning robot can be expressed as:

$$\boldsymbol{M}_{RB}\dot{\boldsymbol{\nu}} + \boldsymbol{C}_{RB}(\boldsymbol{\nu})\boldsymbol{\nu} = \boldsymbol{\tau}_{RB} \tag{6}$$

where $\boldsymbol{\nu} = \left[\boldsymbol{\nu}_1^T, \boldsymbol{\nu}_2^T\right]^T = [u, v, w, p, q, r]^T$ is the generalized velocity vector of the underwater cleaning robot expressed in the body-fixed frame; $\boldsymbol{\tau}_{RB} = \boldsymbol{\tau} = \left[\boldsymbol{\tau}_1^T, \boldsymbol{\tau}_2^T\right]^T = [X, Y, Z, K, M, N]^T$ is the generalized vector of the resultant forces and moments acting on the underwater cleaning robot in the body-fixed frame.

The generalized rigid-body mass matrix $\mathbf{M}_{RB}$ is given by:

$$\boldsymbol{M}_{RB} = \begin{bmatrix} m\boldsymbol{I}_{3\times3} & -m\boldsymbol{S}(\boldsymbol{r}_G) \\ m\boldsymbol{S}(\boldsymbol{r}_G) & \boldsymbol{I}_0 \end{bmatrix} \tag{7}$$

The Coriolis–centripetal matrix is expressed as:

$$\boldsymbol{C}_{RB}(\boldsymbol{\nu}) = \begin{bmatrix} \mathbf{0}_{3\times3} & -m\boldsymbol{S}(\boldsymbol{\nu}_1) - m\boldsymbol{S}(\boldsymbol{\nu}_2)\boldsymbol{S}(\boldsymbol{r}_G) \\ -m\boldsymbol{S}(\boldsymbol{\nu}_1) + m\boldsymbol{S}(\boldsymbol{r}_G)\boldsymbol{S}(\boldsymbol{\nu}_2) & -\boldsymbol{S}(\boldsymbol{I}_0\boldsymbol{\nu}_2) \end{bmatrix} \tag{8}$$

which satisfies the following relationship:

$$\boldsymbol{C}_{RB}(\boldsymbol{\nu}) = -\boldsymbol{C}_{RB}^T(\boldsymbol{\nu}) \forall \boldsymbol{\nu} \in \mathbb{R}^{\mathbf{6}} \tag{9}$$

3.2.2. Analysis of External Forces and Moments

When the underwater cleaning robot moves in the underwater space, without considering the cleaning operation state for the time being, the external forces and moments

acting on it mainly include hydrodynamic forces and moments, environmental disturbance forces and moments induced by underwater waves and currents, and the thrust forces and moments generated by the actuators, namely:

$$\boldsymbol{\tau}_{RB} = \boldsymbol{\tau}_H + \boldsymbol{\tau}_E + \boldsymbol{\tau}_T \tag{10}$$

where $\boldsymbol{\tau}_H$ denotes the hydrodynamic forces and moments, $\boldsymbol{\tau}_E$ denotes the environmental disturbance forces and moments induced by waves and currents, and $\boldsymbol{\tau}_T$ denotes the driving forces and moments generated by the robot's actuators.

(1) Hydrodynamic forces and moments

The hydrodynamic forces and moments can be further divided into three components: added-mass forces and moments, damping forces and moments, and hydrostatic restoring forces and moments caused by gravity and buoyancy.

$$\boldsymbol{\tau_H} = \underbrace{-\boldsymbol{M_A}\dot{\boldsymbol{\nu}} - \boldsymbol{C_A}(\boldsymbol{\nu})\boldsymbol{\nu}}_{\substack{Added-mass\ forces \\ and\ moments}} - \underbrace{\boldsymbol{D}(\boldsymbol{\nu})\boldsymbol{\nu}}_{\substack{Damping\ forces \\ and\ moments}} - \underbrace{\boldsymbol{g}(\boldsymbol{\eta})}_{\substack{Hydrostatic\ restoring\ forces\ and \\ moments\ due\ to\ gravity\ and\ buoyancy}} \tag{11}$$

The added-mass forces and moments are expressed as $\boldsymbol{\tau}_A = -\boldsymbol{M}_A\dot{\boldsymbol{\nu}} - \boldsymbol{C}_A(\boldsymbol{\nu})\boldsymbol{\nu}$. By approximating the robot as a regular geometric body, the following expression can be obtained:

$$\boldsymbol{M}_A = \begin{bmatrix} \boldsymbol{M}_{11} & \boldsymbol{M}_{12} \\ \boldsymbol{M}_{21} & \boldsymbol{M}_{22} \end{bmatrix} = -\mathrm{diag}\left\{ X_{\dot{u}}, Y_{\dot{v}}, Z_{\dot{w}}, K_{\dot{p}}, M_{\dot{q}}, N_{\dot{r}} \right\} \tag{12}$$

$$\boldsymbol{C}_A(\boldsymbol{v}) = \begin{bmatrix} \boldsymbol{0}_{3\times3} & -\boldsymbol{S}(\boldsymbol{M}_{11}\boldsymbol{\nu}_1 + \boldsymbol{M}_{12}\boldsymbol{\nu}_2) \\ -\boldsymbol{S}(\boldsymbol{M}_{11}\boldsymbol{\nu}_1 + \boldsymbol{M}_{12}\boldsymbol{\nu}_2) & -\boldsymbol{S}(\boldsymbol{M}_{21}\boldsymbol{\nu}_1 + \boldsymbol{M}_{22}\boldsymbol{\nu}_2) \end{bmatrix} = \begin{bmatrix} 0 & 0 & 0 & 0 & -Z_{\dot{w}}w & Y_{\dot{v}}v \\ 0 & 0 & 0 & Z_{\dot{w}}w & 0 & -X_{\dot{u}}u \\ 0 & 0 & 0 & -Y_{\dot{v}}v & X_{\dot{u}}u & 0 \\ 0 & -Z_{\dot{w}}w & Y_{\dot{v}}v & 0 & -N_{\dot{r}}r & M_{\dot{q}}q \\ Z_{\dot{w}}w & 0 & -X_{\dot{u}}u & N_{\dot{r}}r & 0 & -K_{\dot{p}}p \\ -Y_{\dot{v}}v & X_{\dot{u}}u & 0 & -M_{\dot{q}}q & K_{\dot{p}}p & 0 \end{bmatrix} \tag{13}$$

where $X_{\dot{u}}, Y_{\dot{v}}, Z_{\dot{w}}, K_{\dot{p}}, M_{\dot{q}}, N_{\dot{r}}$ are the added-mass coefficients, which are obtained through the CFD simulations described in the following section.

The damping force $\boldsymbol{\tau}_D$ is one of the fundamental components of the fluid forces acting on the robot during its motion. The viscous resistance in six degrees of freedom is described using the second-order Taylor series expansion of the Morison equation, with higher-order terms neglected. Accordingly, the viscous-force coefficient matrix can be expressed as:

$$\boldsymbol{D}(\boldsymbol{v}) = -\begin{bmatrix} X_u + X_{u|u|}|u| & 0 & 0 & 0 & 0 & 0 \\ 0 & Y_v + Y_{v|v|}|v| & 0 & 0 & 0 & 0 \\ 0 & 0 & Z_w + Z_{w|w|}|w| & 0 & 0 & 0 \\ 0 & 0 & 0 & K_p + K_{p|p|}|p| & 0 & 0 \\ 0 & 0 & 0 & 0 & M_q + M_{q|q|}|q| & 0 \\ 0 & 0 & 0 & 0 & 0 & N_r + N_{r|r|}|r| \end{bmatrix} \tag{14}$$

Similarly, the damping-force coefficients involved are also obtained through CFD simulations.

Gravity and buoyancy are referred to as hydrostatic restoring forces in fluid mechanics, acting at the center of gravity and the center of buoyancy of the underwater cleaning robot, respectively. Moreover, since the center of gravity and the center of buoyancy do not coincide, when the underwater cleaning robot undergoes pitch and roll motions, gravity

and buoyancy no longer act along the same vertical line, thereby generating restoring moments. Therefore, the six-dimensional restoring force vector can be obtained as:

$$g(\eta) = \begin{bmatrix} (W-B)s\theta \\ -(W-B)c\theta s\phi \\ -(W-B)c\theta c\phi \\ -(y_G W - y_G B)c\theta c\phi + (z_G W - z_B B)c\theta s\phi \\ (z_G W - z_B B)s\theta + (x_G W - x_B B)c\theta c\phi \\ -(x_G W - x_B B)c\theta s\phi - (y_G W - y_B B)s\theta \end{bmatrix} = \begin{bmatrix} (W-B)s\theta \\ -(W-B)c\theta s\phi \\ -(W-B)c\theta c\phi \\ -z_B B c\theta s\phi \\ -z_B B s\theta \\ 0 \end{bmatrix} \quad (15)$$

(2) Environmental disturbance induced by ocean currents

The underwater cleaning robot is subject to current disturbances in its operating environment. Since the environmental disturbance forces and moments τ_E induced by waves and currents are difficult to express explicitly in mathematical form, the effect of ocean currents is modeled by introducing the relative flow velocity into the fluid-force terms of the dynamic model. In this way, the current-induced forces and moments τ_E are incorporated into the dynamic model of the underwater cleaning robot.

Assume that the current velocity in the inertial frame is $\nu_s = [u_s, v_s, w_s]^T$, and the corresponding velocity in the body-fixed frame is $\nu_c = [u_c, v_c, w_c]^T$. The transformation relationship is given by $\nu_c = J_1^{-1}(\eta_2)\nu_s$. Accordingly, the velocity of the robot relative to the current in the body-fixed frame can be expressed as:

$$\nu_1^r = \nu_1 - \nu_c = \begin{bmatrix} u - u_c \\ v - v_c \\ w - w_c \end{bmatrix} = \begin{bmatrix} u_r \\ v_r \\ w_r \end{bmatrix} \quad (16)$$

By replacing ν_1 in the robot dynamic equations under still-water conditions with the relative velocity of the robot with respect to the current, denoted as ν_1^r, the generalized velocity vector ν_r can be obtained, where $\dot{\nu}_r = \dot{\nu}$.

(3) Driving forces and moments

Since the cleaning operation state of the underwater cleaning robot is not considered in this study, under conventional three-dimensional motion, the robot uses only the propeller thrusters as actuators for motion driving and control, while the magnetic adhesion drive wheels remain inactive. The driving forces and moments generated by different actuators can be expressed as:

$$\tau_T = \tau_{HP1\&HP2} + \tau_{VP1\&VP2} \quad (17)$$

where $\tau_{\mathrm{HP1\&HP2}}$ denotes the resultant forces and moments generated by the left and right horizontal propeller thrusters, and $\tau_{\mathrm{VP1\&VP2}}$ denotes the thrust forces and moments generated by the two vertical propeller thrusters.

The thrust of the propeller thruster is generated by the rotation of the propeller driven by the motor. A series of simulation data for the thrust T and torque Q can be obtained through CFD simulations, based on which the thrust coefficient K_T and torque coefficient K_Q are calculated using Equation (18).

$$\begin{cases} T = K_T \rho n|n| D^4 \\ Q = K_Q \rho n|n| D^5 \end{cases} \quad (18)$$

where ρ denotes the fluid density, n denotes the rotational speed of the propeller, and D denotes the propeller diameter. The simulation data are analyzed using least-squares fitting to obtain the relationship curves between the advance coefficient and K_T and K_Q [23]. The

advance coefficient is calculated as follows, where the rotational speed is expressed in rev/s:

$$J = \frac{U}{nD} \tag{19}$$

where $U = \|\boldsymbol{\nu}_1\| = \sqrt{u^2 + v^2 + w^2}$ denotes the translational velocity of the thruster. By substituting the fitted $J - K_T$ and $J - K_Q$ curves back into Equation (18), the relationship curves of the thrust T and torque Q with respect to the advance coefficient J and rotational speed n can finally be obtained.

Taking the force and moment generated by the right horizontal propeller thruster as an example, its thrust can be expressed as $T_{\mathrm{HP2}}\boldsymbol{e}_1$, and the corresponding moment is given by $Q_{HP2}\mathbf{e}_1 + \boldsymbol{S}(\mathbf{r}_{HP2})T_{HP2}\mathbf{e}_1$. Here, $\boldsymbol{r}_{\mathrm{Hp2}}$ denotes the position vector from the origin of the body-fixed frame to the thrust application center of the right horizontal propeller thruster, and $\boldsymbol{S}(\boldsymbol{r}_{\mathrm{HP2}})T_{\mathrm{HP2}}\boldsymbol{e}_1$ represents the moment generated by the thrust $T_{\mathrm{HP2}}\boldsymbol{e}_1$ about the body-fixed frame. Since $\|Q_{HP2}\mathbf{e}_1\| \ll \|S(\mathbf{r}_{HP2})T_{HP2}\mathbf{e}_1\|$, the propeller-induced torque $Q_{\mathrm{HP2}}\boldsymbol{e}_1$ can be neglected. Therefore, the resultant driving forces and moments generated by the left and right horizontal propeller thrusters can be expressed as:

$$\begin{aligned}\boldsymbol{\tau}_{\mathrm{HP1\&HP2}} &= \begin{bmatrix} (T_{\mathrm{HP1}} + T_{\mathrm{HP2}})\boldsymbol{e}_1 \\ S(\boldsymbol{r}_{\mathrm{HP1}})T_{\mathrm{HP1}}\boldsymbol{e}_1 + S(\boldsymbol{r}_{\mathrm{HP2}})T_{\mathrm{HP2}}\boldsymbol{e}_1 \end{bmatrix} \\ &= \begin{bmatrix} \boldsymbol{e}_1 & \boldsymbol{e}_1 \\ \boldsymbol{S}(\boldsymbol{r}_{\mathrm{HP1}})\boldsymbol{e}_1 & \boldsymbol{S}(\boldsymbol{r}_{\mathrm{HP2}})\boldsymbol{e}_1 \end{bmatrix} \begin{bmatrix} \rho D^4 K_{T,\mathrm{HP1}} & 0 \\ 0 & \rho D^4 K_{T,\mathrm{HP2}} \end{bmatrix} \begin{bmatrix} n_{\mathrm{HP1}}|n_{\mathrm{HP1}}| \\ n_{\mathrm{HP2}}|n_{\mathrm{HP2}}| \end{bmatrix}\end{aligned} \tag{20}$$

where n_{HP1} and n_{HP2} denote the rotational speeds of the left and right horizontal propeller thrusters, respectively. Similarly, the thrust forces and moments provided by the vertical thrusters can be expressed as follows:

$$\boldsymbol{\tau}_{\mathrm{VP1\&VP2}} = \begin{bmatrix} \boldsymbol{e}_3 & \boldsymbol{e}_3 \\ \boldsymbol{S}(\boldsymbol{r}_{\mathrm{VP1}})\boldsymbol{e}_3 & \boldsymbol{S}(\boldsymbol{r}_{\mathrm{VP2}})\boldsymbol{e}_3 \end{bmatrix} \begin{bmatrix} \rho D^4 K_{T,\mathrm{VP1}} & 0 \\ 0 & \rho D^4 K_{T,\mathrm{VP2}} \end{bmatrix} \begin{bmatrix} n_{\mathrm{VP1}}|n_{\mathrm{VP1}}| \\ n_{\mathrm{VP2}}|n_{\mathrm{VP2}}| \end{bmatrix} \tag{21}$$

3.2.3. Dynamics Model and Model Limitations Description

Based on the above analysis, the dynamic model of the underwater cleaning robot moving in three-dimensional space under ocean-current disturbances can finally be obtained.

$$\boldsymbol{M}_{RB}\dot{\boldsymbol{\nu}}_r + \boldsymbol{C}_{RB}(\boldsymbol{\nu}_r)\boldsymbol{\nu}_r = \boldsymbol{\tau}_{\boldsymbol{T}} - \boldsymbol{M}_A\dot{\boldsymbol{\nu}}_r - \boldsymbol{C}_A(\boldsymbol{\nu}_r)\boldsymbol{\nu}_r - \boldsymbol{D}(\boldsymbol{\nu}_r)\boldsymbol{\nu}_r - \boldsymbol{g}(\boldsymbol{\eta}) \tag{22}$$

Further rearrangement yields:

$$\underbrace{(\boldsymbol{M}_{RB} + \boldsymbol{M}_A)}_{\boldsymbol{M}}\dot{\boldsymbol{\nu}}_r + \underbrace{(\boldsymbol{C}_{RB}(\boldsymbol{\nu}_r) + \boldsymbol{C}_A(\boldsymbol{\nu}_r))}_{\boldsymbol{C}(\boldsymbol{\nu}_r)}\boldsymbol{\nu}_r + \boldsymbol{D}(\boldsymbol{\nu}_r)\boldsymbol{\nu}_r + \boldsymbol{g}(\boldsymbol{\eta}) = \boldsymbol{\tau}_{\boldsymbol{T}} \tag{23}$$

where $\boldsymbol{M}$ is the total mass matrix, and $\boldsymbol{C}(\boldsymbol{\nu}_r)$ is the total Coriolis and centripetal matrix.

We would like to further clarify that the diagonalization of the added-mass matrix $\boldsymbol{M}_A$ and the damping matrix $\boldsymbol{D}$ in this paper is based on the following analyses:

(1) Geometric symmetry analysis

As shown in Table 1, the four thrusters and wheels are mounted symmetrically on the left and right sides. Consequently, the robot possesses strict geometric symmetry in the x-z plane and approximate symmetry in the x-y and y-z planes. The main hull, frame, and internal equipment (battery packs, control cabin) have their mass concentrated near the geometric center. Although external attachments such as wheels and thruster pipelines cause slight local asymmetries, their mass accounts for a relatively small proportion of the total mass and thus has a limited effect on the overall mass distribution.

(2) Hydrodynamic symmetry analysis

In the CFD computations, the overall hydrodynamic coefficients are dominated by the components in the same direction, while the cross-coupling effects are relatively weak. We will further quantify the magnitude of the cross-coupling terms through analysis of the CFD data.

(3) Statement of model limitations

It should be noted that complete diagonalization is an idealizing assumption. In practice, due to the non-perfect symmetry of the wheels, thruster pipelines, and internal equipment layout, off-diagonal coupling terms theoretically exist in the hydrodynamic matrices. In this paper, we neglect these off-diagonal coupling terms as higher-order small quantities. This assumption is reasonable for low-speed robot motion and small attitude angles, but it may lead to model inaccuracies under other motion conditions.

It should be noted that the current dynamic model addresses the robot's free-navigation condition without cleaning operation. The cleaning process involves complex hydrodynamic effects, namely jet reaction forces, wall proximity effects, and fluid–structure interactions between the cleaning brushes and fouled surface, which are excluded from this model due to the substantial increase in CFD computational cost and model complexity they would entail. Consequently, the present model is applicable to transit and positioning maneuvers in open water, while cleaning-operation dynamics remain an important direction for future research.

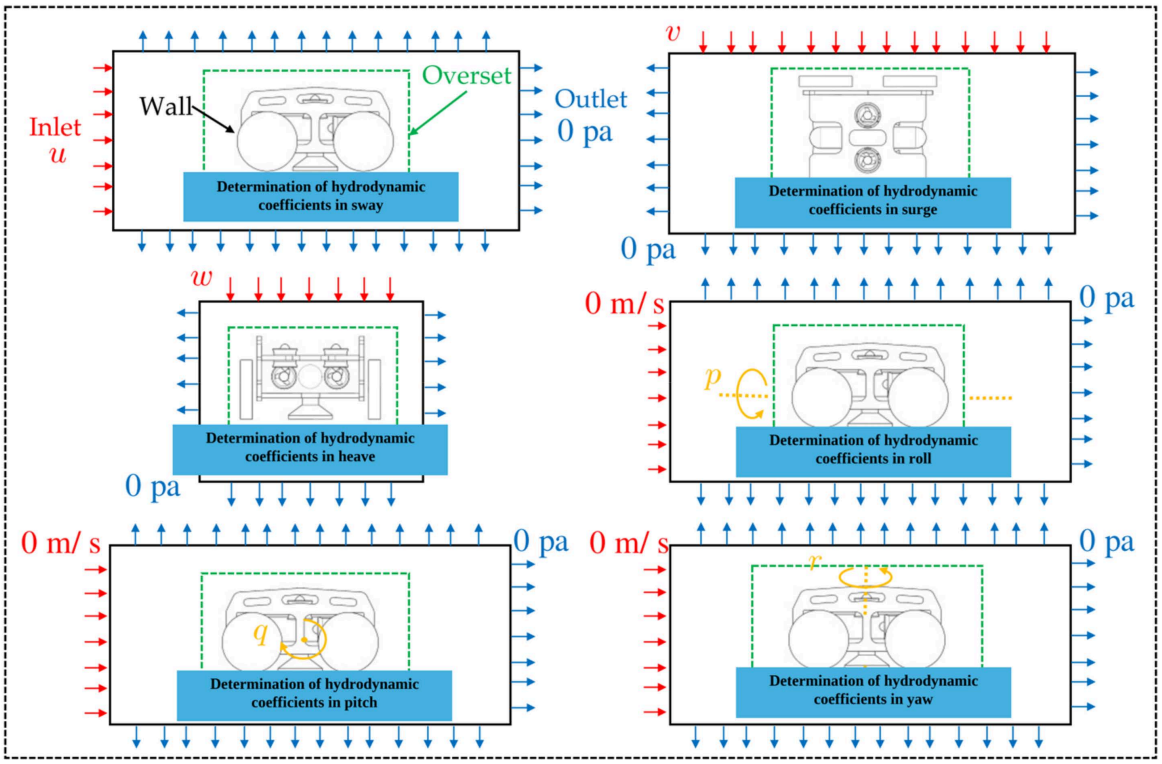
4. Hydrodynamic Characteristic Analysis of the Jacket Cleaning Robot

The theoretical model of the underwater cleaning robot moving in three-dimensional space has been derived in the preceding section. Since some hydrodynamic coefficients and propeller thrust coefficients involved in the model remain unknown, this section determines these unknown parameters using CFD simulations based on the commercial fluid dynamics software ANSYS Fluent 2025 R2, thereby completing the theoretical model.

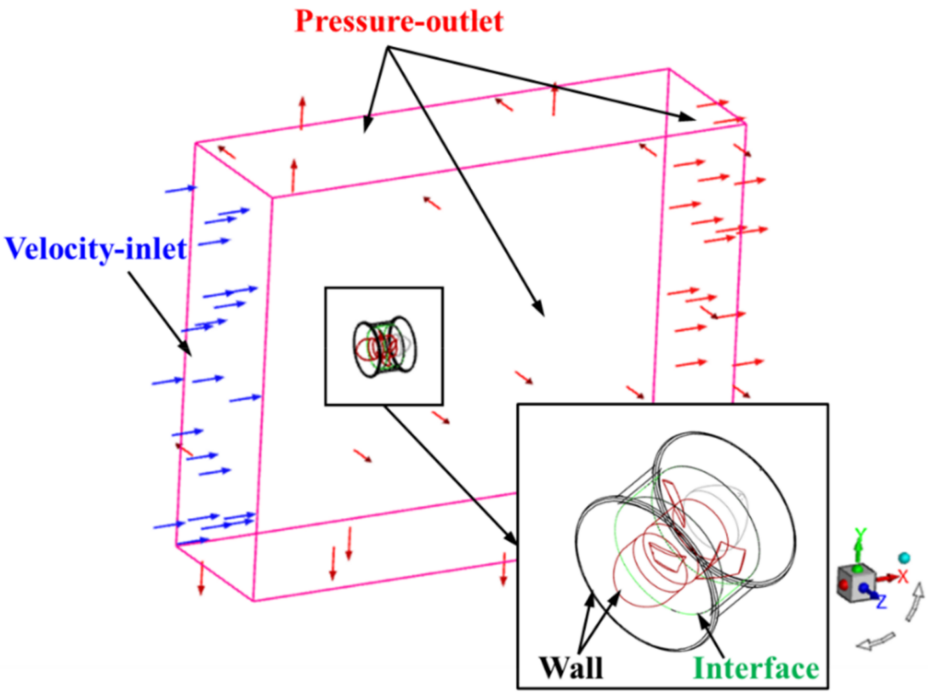
4.1. Construction of the Numerical Computational Domain and Solver Settings

For the damping-force coefficients and added-mass coefficients of the underwater cleaning robot, the overset grid technique is adopted to realize the motion of the robot with different degrees of freedom in the flow field. To apply the overset grid method, a background mesh and a component mesh are established separately. A component mesh region is generated around the robot, and this region is embedded within the large-scale background flow domain. The default initial boundary conditions are set as follows: the inlet is defined as a velocity inlet with an inlet velocity of 0 m/s; the outlet is defined as a pressure outlet with a gauge pressure of 0 Pa; all external surfaces of the robot are set as no-slip walls; and the overlapping region is defined as an overset interface.

To solve the damping-force and moment coefficients, as shown in Figure 5a, for the sway, surge, and heave motions of the robot, the robot position is fixed, and the relative motion between the robot and the surrounding fluid domain is equivalently represented by varying the inlet velocity at the velocity inlet. Specifically, the inlet velocity is prescribed as u_{in} m/s in different directions, while the pressure outlet is maintained at a gauge pressure of 0 Pa, and the remaining boundary conditions are kept consistent with those described above. For the roll, pitch, and yaw motions of the robot, steady-state calculations are performed, and the moving reference frame method is used to define the relative rotational velocity of the overset region around the robot. In this case, the inlet velocity is set to 0 m/s, the pressure outlet gauge pressure is set to 0 Pa, and the other boundary conditions remain the same as the default settings.



(**a**)



(**b**)

Figure 5. Boundary conditions applied to the computational domain. (**a**) Flow field and boundary conditions for identifying the hydrodynamic coefficients of the robot body. (**b**) Flow field and boundary conditions for identifying the thrust coefficients of the propeller thruster.

For solving the added-mass force and moment coefficients, transient calculations and the mesh motion technique are adopted. The component mesh region is prescribed with a small-amplitude sinusoidal velocity, either translational (in m/s) or rotational (in rad/s), expressed as $v_0 = 0.01\sin(2\pi t)$. Although robots have both added mass forces

and fluid resistance when moving, when their speed is 0, at this point they only have the added mass force, and the coefficient of the added mass force is equal to the force divided by the acceleration (the derivative of the speed). Additionally, existing studies [24] have demonstrated that the added mass coefficients obtained through this "forced oscillation" method are independent of the oscillation frequency; therefore, we employed only a single oscillation frequency of 1 Hz. The forces and moments generated in each degree of freedom can then be fitted in the following first-order Fourier series form.

$$\begin{cases} F_i = a_i \cdot sin(2\pi t) + b_i cos(2\pi t) \\ M_i = c_i \cdot sin(2\pi t) + d_i cos(2\pi t) \end{cases} \tag{24}$$

Thus, the coefficients of added mass forces and moments can be calculated according to the following formula.

$$\begin{cases} C_{FA,i} = \frac{b_i cos(2\pi t)}{\dot{v}_0} \\ C_{MA,i} = \frac{d_i cos(2\pi t)}{\dot{v}_0} \end{cases} \tag{25}$$

where $C_{FA,i}$ and $C_{MA,i}$ respectively represent the added mass forces and moment coefficients at each degree of freedom. After removing the sinusoidal term that has a fixed relationship with the motion velocity, the remaining cosine term corresponds to the added-mass forces and moments. In addition, it should be noted that the justification for using a single oscillation frequency for parameter identification in this study rests on the specific low-Keulegan-Carpenter number regime (KC < 1). Within this low-KC range, the frequency dependence of added-mass and damping coefficients for bluff-body geometries is known to be relatively weak. Experimental investigations on oscillating bluff bodies have demonstrated that, at low KC numbers, the dependence of added mass and damping on oscillation frequency is negligible, and the hydrodynamic coefficients become essentially frequency-independent beyond a certain frequency threshold [25]. Therefore, the single-frequency identification adopted herein is considered representative of the average dynamic behavior over the operational range. This assumption, however, is not extended to higher KC numbers or large-amplitude oscillations, where frequency effects and nonlinear vortex-shedding phenomena may become non-negligible.

For determining the thrust coefficients of the propeller thrusters, as shown in Figure 5b, the entire external flow domain of the thruster is first constructed, and the rotating domain of the propeller is treated separately. The inlet is defined as a velocity inlet with an inlet velocity of u_{in} m/s, where different inlet velocities are prescribed for different cases. The outlet is defined as a pressure outlet with a gauge pressure of 0 Pa. The external surfaces of the thruster are specified as no-slip walls, and the cylindrical surface of the rotating domain is defined as an interface. The regional motion is still defined using a steady-state calculation combined with the moving reference frame method.

To ensure the effective solution of the governing equations, the following numerical settings are adopted: A pressure-based solver with an absolute velocity formulation is used. The Reynolds number range, calculated based on the main body characteristic dimensions (length, width, height) of the robot, the inlet speed, and the fluid dynamic viscosity, is 3.93×10^4 to 1.3×10^5, and the flow is in a turbulent state. The SST k-ω turbulence model, namely the shear stress transport model, is selected. This model combines the k-ω formulation in the near-wall region for superior boundary-layer resolution with the k-ε formulation in the outer flow, while offering enhanced predictive accuracy for adverse pressure gradients and flow separation. These features are particularly important for the bluff-body flow around underwater robots. The coupled algorithm is employed for pressure-velocity coupling, and the remaining solution control parameters are kept at their default settings. During the simulation, the computation is considered converged and can

be terminated when the residual of the continuity equation and the momentum equations fall below 10^{-6}, and the monitored values of forces, moments, and their corresponding coefficients exhibit fluctuations within 2%.

4.2. Numerical Solution

4.2.1. Mesh Independence Verification

Before the formal simulation calculations, to improve the solution accuracy, a mesh independence study was performed to determine the most appropriate mesh size. First, the background mesh and component mesh of the two computational domains shown in Figure 5 were each divided into three size levels, while requiring that the minimum orthogonal quality of all meshes be no less than 0.3. Accordingly, three levels of volume mesh models were generated (coarse, medium, and fine). The number of cells and the mesh size parameters for each level are listed in Table 3.

Table 3. The results of the mesh independence verification.

Verified Items	Level	Background Mesh		Component Mesh		Result	Error
		Local Minimum Size (mm)	Number	Local Minimum Size (mm)	Number		
Hydrodynamic coefficients	Coarse	30	498,461	8	837,924	919.89	10.51%
	Coarser	20	2,337,386	4	4,498,732	843.39	1.32%
	Fine	10	11,276,743	2	23,634,136	832.40	0
Thrust coefficients	Coarse	4	102,362	1	11,907	26.22	7.33%
	Coarser	2	453,784	0.5	46,343	24.65	0.90%
	Fine	1	2,281,414	0.25	216,567	24.43	0

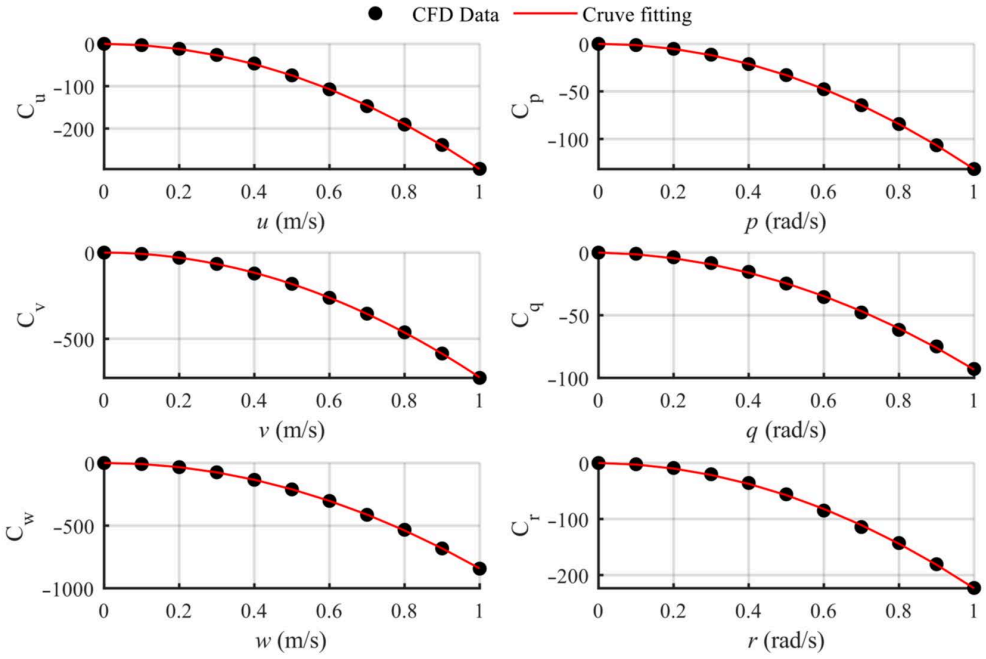
The steady-state solutions of the heave damping coefficient and the thruster thrust coefficient (at an inlet velocity of 0.25 m/s and a rotational speed of 3000 RPM) were used as metrics to compare the computational results from different mesh levels in the two flow domains. The results obtained with the finest mesh and the smallest time step were taken as the reference values, and the errors for the other mesh and time-step levels were calculated. As shown in Table 3, under both verification conditions for the two flow domains, the error of the medium-mesh level results relative to the fine-mesh results was less than 2%, indicating acceptable accuracy. Therefore, to reduce the computational cost while ensuring calculation accuracy, the medium-mesh level was selected for all subsequent simulations.

4.2.2. Hydrodynamic Coefficients of the Robot

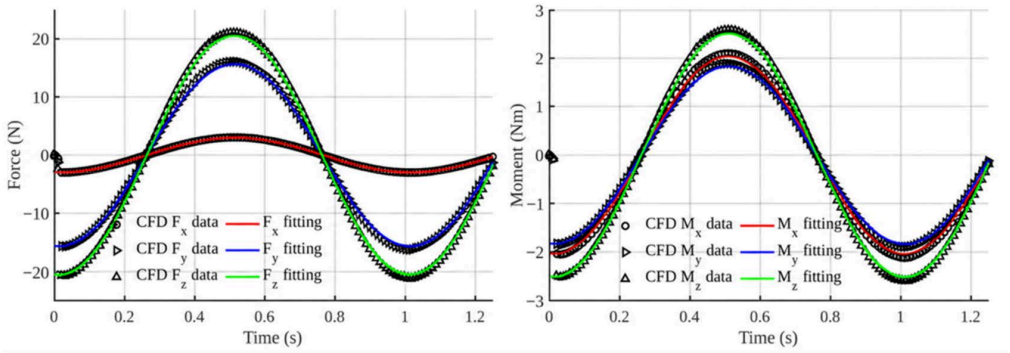
In the analysis of the damping force and moment coefficients of the underwater cleaning robot, the component mesh region of the robot was prescribed with equivalent translational or rotational motions with magnitudes ranging from 0 to 1 m/s or rad/s, respectively. The forces and moments in each degree of freedom were monitored. The steady-state calculation reached convergence after approximately 300 iterations. As shown in Figure 6a, the curves obtained by quadratic polynomial fitting are smooth, and the R^2 values of the fitted curves for all degrees of freedom are greater than 0.99.

In the analysis of the added-mass force and moment coefficients of the underwater cleaning robot, the transient computational results of the forces and moments in each degree of freedom are shown in Figure 6b. The coefficients of the fitted curves are listed in Table 4, and the corresponding R^2 values are approximately 0.97, indicating good fitting accuracy. The added-mass force and moment coefficients in each degree of freedom can be obtained by dividing the cosine term of the fitted curve by the acceleration function obtained from the time derivative of the prescribed motion velocity, namely $0.01 \cdot 2\pi\cos(2\pi t)$. In addition, as

shown in Table 5, to assess the magnitude of the off-diagonal coupling terms, we analyzed the CFD data under multi-DOF coupled oscillations. Specifically, for the pure heave oscillation case, for example, the responses of the rolling moment and pitching moment were monitored. The computational results show that the rolling-moment amplitude $|M_x|_{max}$ = 0.16 N·m, which is two orders of magnitude smaller than the primary heave force amplitude $|F_z|_{max}$ = 21.1 N; the pitching-moment response $|M_y|_{max}$ = 0.035 N·m is also negligible. Similar behavior is observed for the other degrees of freedom. This demonstrates that, within the operating conditions studied in this paper, the off-diagonal coupling effects are indeed small, and thus the diagonalization assumption is reasonable.



(**a**) Fitting of damping forces and moments coefficients



(**b**) Fitting of added-mass forces and moments

Figure 6. Fitting results of hydrodynamic forces and moments.

Table 4. Fitted curve coefficients of added-mass forces and moments.

	F_x	F_y	F_z	M_x	M_y	M_z
a_i or c_i	−0.2882	−1.2356	−1.7236	−0.1357	−0.1170	−0.1768
b_i or d_i	−2.9191	−15.5967	−20.4713	−2.0344	−1.8246	−2.5030
R^2	0.9740	0.9702	0.9714	0.9690	0.9692	0.9688

Table 5. The amplitudes of forces and moments acting on the system during small-amplitude sinusoidal motion in each degree of freedom.

	$\lvert F_x \rvert_{max}$	$\lvert F_y \rvert_{max}$	$\lvert F_z \rvert_{max}$	$\lvert M_x \rvert_{max}$	$\lvert M_y \rvert_{max}$	$\lvert M_z \rvert_{max}$
Surge	3.01	0.0016	0.052	0.0013	0.23	0.0015
Sway	0.0015	16.10	0.023	1.45	0.00094	0.014
Heave	0.050	0.21	21.1	0.16	0.035	0.00082
Roll	0.0011	0.044	0.16	2.11	0.00094	0.0076
Pitch	0.23	0.0075	0.032	0.0010	1.89	0.017
Yaw	0.012	0.014	0.00059	0.0079	0.017	2.59

Finally, the hydrodynamic coefficients of the underwater cleaning robot are obtained, as listed in Table 6. In Table 6, Z_w is positive while all other linear damping coefficients are negative. It should be noted that this positive sign does not indicate a genuine asymmetric flow effect in the heave direction; rather, it is a mathematical outcome of the equivalent-linearization fitting procedure. Because a quadratic damping model is adopted in this work, the fitted linearized damping coefficient is not an independent physical constant; its sign and magnitude depend on the phase relationship between the velocity and the corresponding degree of freedom within the selected frequency band. Consequently, this positive value should not be interpreted as negative physical dissipation, nor does it affect the predictive performance of the model within the operational range.

Table 6. Hydrodynamic coefficient values.

Coefficients of Damping Forces and Moments	Coefficient	X_u	$X_{u\lvert u\rvert}$	Y_v	$Y_{v\lvert v\rvert}$	Z_w	$Z_{w\lvert w\rvert}$
	value	−2.01	−293.8	−5.08	−718.57	3.02	−844.9
	Coefficient	K_p	$K_{p\lvert p\rvert}$	M_q	$M_{q\lvert q\rvert}$	N_r	$N_{r\lvert r\rvert}$
	value	−0.148	−131.56	−4.73	−88.61	−5.96	−217.62
Coefficients of added-mass forces and moments	Coefficient	$X_{\dot{u}}$	$Y_{\dot{v}}$	$Z_{\dot{w}}$	$K_{\dot{p}}$	$M_{\dot{q}}$	$N_{\dot{r}}$
	value	−46.46	−248.23	−325.81	−32.38	−29.04	−39.84

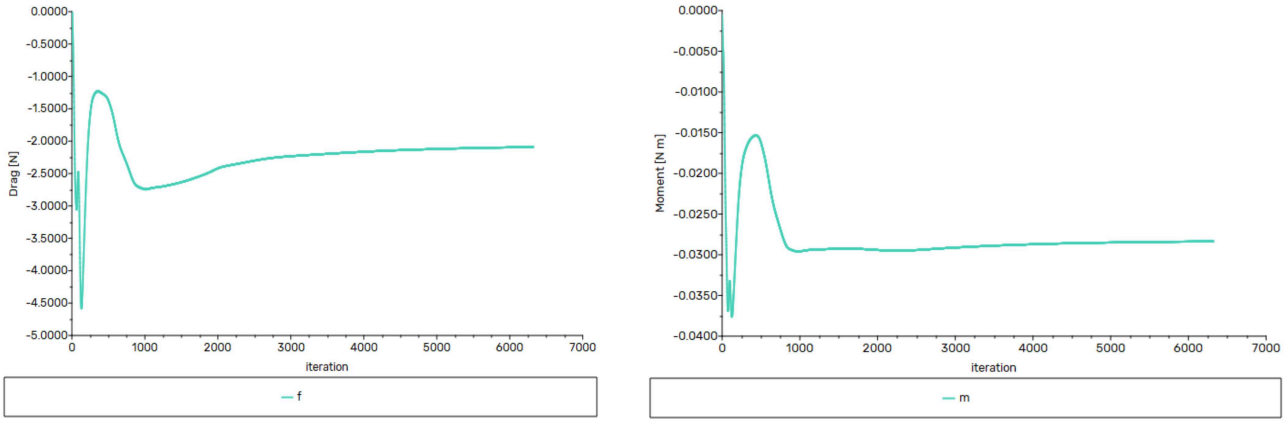
4.2.3. Propeller Thrust Coefficient

As shown in Figure 7, the steady-state iterative calculation curves of the thruster thrust and torque are obtained at an inlet velocity of 0.25 m/s and a rotational speed of 1000 rpm. The calculation tends to reach a steady state after more than 6000 iterations. CFD simulations of the thruster are then carried out under different rotational speeds and inlet velocities.

The results are listed in Table 7. Under different rotational speeds and inlet velocities, the thruster exhibits different advance coefficients J, thrust values, and torque values. Furthermore, the CFD data are plotted and fitted to obtain the propeller characteristic curves, as shown in Figure 8. The thrust coefficient K_T, torque coefficient K_Q, and efficiency η of the propeller are fitted using quadratic polynomials, as expressed in Equation (26). The corresponding R^2 values are all greater than 0.96, satisfying the accuracy requirement. Furthermore, we utilized the publicly available thrust–PWM-RPM curve data from the T200 thruster manufacturer to compare with the static thrust computed by CFD at zero inflow velocity. As shown in Figure 9, the CFD predictions deviate from the manufacturer data by 7.8%, 14.3%, and 12.2% at 1000, 2000, and 3000 RPM, respectively. For marine propeller thrust prediction in the moderate-load range, errors within 10–15% are generally considered acceptable in comparable CFD studies [26]. The error tends to increase with rotational speed, which can be attributed to the growing influence of unsteady blade-wake interactions and turbulence modeling limitations at higher advance ratios. The overall

good agreement between the CFD predictions and the experimental values across different rotational speeds demonstrates the reliability of the present CFD results.

$$\begin{cases} K_T = -0.3299J^2 - 0.2771J + 0.304 \\ K_Q = -0.239J^2 - 0.096J + 0.432 \\ \eta = -4.2724J^2 + 2.7332J - 0.1531 \end{cases} \quad (26)$$



(**a**) Thrust (**b**) Torque

Figure 7. Thrust and torque curves of the thruster at an inlet velocity of 0.25 m/s and a rotational speed of 1000 rpm.

Table 7. Calculated advance coefficient, thrust, and torque of the thruster.

	J			T			Q		
n (RPM) u (m/s)	**1000**	**2000**	**3000**	**1000**	**2000**	**3000**	**1000**	**2000**	**3000**
0.25	0.197	0.099	0.066	2.09	10.35	24.65	0.0284	0.120	0.275
0.50	0.395	0.197	0.132	1.33	8.90	22.38	0.0258	0.113	0.258
0.75	0.592	0.296	0.197	0.33	7.37	20.45	0.0208	0.108	0.252
1.00	0.789	0.395	0.263	−1.09	5.71	18.13	0.0144	0.101	0.245

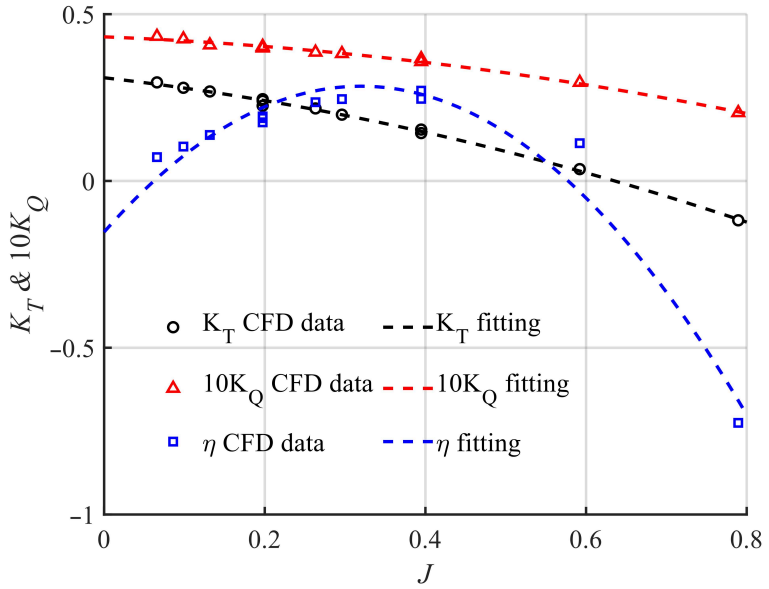


Figure 8. Propeller characteristic curves (force and torque coefficients and efficiency curves).

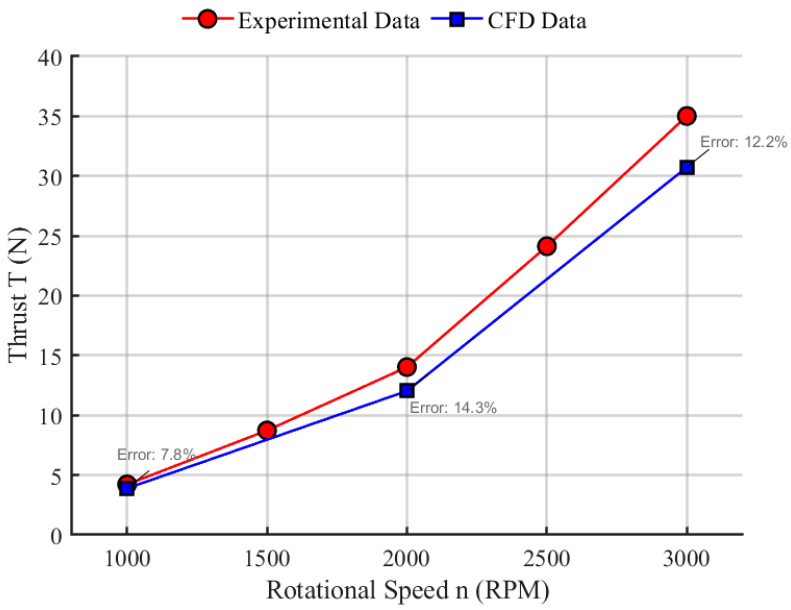


Figure 9. Comparison of thrust between CFD and experimental data.

5. Conclusions

This paper addresses the demand for removing marine biofouling from the surfaces of offshore platform jackets and designs an underwater cleaning robot adopting a combined configuration of a wheeled chassis, thrust-based adhesion, and magnetic adhesion. The robot has an overall mass of approximately 150 kg and overall dimensions of 1.3 m × 1.2 m × 0.4 m. It is equipped with four T200 propeller thrusters and a magnetic adhesion wheeled chassis, enabling stable attachment and locomotion under non-uniform tubular-diameter conditions. This study presents a 6-DOF dynamic modeling framework for an underwater jacket cleaning robot, with hydrodynamic and thruster coefficients identified through systematic CFD simulations. The main contributions and findings are summarized as follows.

The kinematic and dynamic models are formulated in both inertial and body-fixed coordinate systems following the Fossen/SNAME framework. The hydrodynamic forces, including added-mass effects, damping forces, and hydrostatic restoring forces, are incorporated into the equations of motion. Through CFD simulations employing overset grids, moving reference frames, and forced oscillation techniques, the damping coefficients, added-mass coefficients, and thruster thrust and torque coefficients are identified for each degree of freedom. The quadratic polynomial fittings for the damping forces and moments yield coefficients of determination greater than 0.99, while those for the added-mass forces and moments are approximately 0.97, and the propeller characteristic curve fittings exceed 0.96. These statistical indicators confirm the internal consistency of the CFD-based identification process.

However, this paper simplifies the hydrodynamic matrix to a diagonal form based on the approximate symmetry of the geometry and mass distribution. This assumption is reasonable under low-speed, small-perturbation conditions, but strict symmetry does not actually hold. In future work, we will identify the full 6 × 6 coupled matrix through coupled-oscillation CFD simulations or tank experiments, so as to further refine and validate the model presented herein. Additionally, the current dynamic model is applicable to the robot's free-navigation condition without cleaning operation, as the complex hydrodynamic effects induced by jet reaction forces and wall proximity during cleaning are

excluded. The extension of this model to include cleaning-operation dynamics will also be addressed in future work.

This study provides a complete theoretical model and simulation-data support for motion control and operational stability analysis of underwater cleaning robots, and offers engineering reference value for improving the automation level and operational safety of offshore platform jacket maintenance.

Author Contributions: Conceptualization, J.Y., D.L. and W.S.; methodology, W.S. and Y.M. (Yanjun Ma); software, Y.C. and Y.M. (Yanjun Ma); validation, J.Y., D.L. and Y.C.; formal analysis, J.Y. and Y.M. (Yanjun Ma); investigation, Y.M. (Yanjun Ma); resources, J.Y. and Y.C.; data curation, D.L. and W.S.; writing—original draft preparation, J.Y. and D.L.; writing—review and editing, X.C., Y.Z. and Y.M. (Yongfei Ma); visualization, X.C. and Y.M. (Yongfei Ma); supervision, Y.M. (Yongfei Ma) and Y.Z.; project administration, Y.Z.; funding acquisition, Y.Z. All authors have read and agreed to the published version of the manuscript.

Funding: This research was funded by the Fundamental Research Funds for the Central Universities, grant number 26CX02012A; and the Research Funds of Guangdong Power Grid Co., Ltd., grant number GDKJXM20240661. The APC was funded by the Fundamental Research Funds for the Central Universities, grant number 26CX02012A.

Institutional Review Board Statement: Not applicable.

Informed Consent Statement: Not applicable.

Data Availability Statement: Data is contained within this article.

Conflicts of Interest: Author Wenxing Sun and Duanjiao Li were employed by the company Guangdong Power Grid Co., Ltd., Guangzhou 510030, China. Author Junwen Yao, Yun Chen and Yanjun Ma were employed by the company Electric Power Research Institute of Guangdong Power Grid Co., Ltd., Guangzhou 510030, China. The remaining authors declare that the research was conducted in the absence of any commercial or financial relationships that could be construed as a potential conflict of interest.

References

1. Hadžić, N.; Jovanović, I.; Vladimir, N. Biofouling of ships and offshore structures: Research trends and future pathways. *Ocean Eng.* **2026**, *347*, 123988. [CrossRef]
2. Poozesh, P.; Nieto, F.; Fernández, P.M.; Ríos, R.; Díaz-Casás, V. Biofouling on Offshore Wind Energy Structures: Characterization, Impacts, Mitigation Strategies, and Future Trends. *J. Mar. Sci. Eng.* **2025**, *13*, 1363. [CrossRef]
3. Maduka, M.; Schoefs, F.; Thiagarajan, K.; Bates, A. Hydrodynamic effects of biofouling-induced surface roughness—Review and research gaps for shallow water offshore wind energy structures. *Ocean Eng.* **2023**, *272*, 113798. [CrossRef]
4. Marty, A.; Schoefs, F.; Damblans, G.; Facq, J.-V.; Gaurier, B.; Germain, G. Experimental study of two kinds of hard marine growth effects on the hydrodynamic behavior of a cylinder submitted to wave and current loading. *Ocean Eng.* **2022**, *263*, 112194. [CrossRef]
5. Schoefs, F.; Bakhtiari, A.; Ameryoun, H. Evaluation of Hydrodynamic Force Coefficients in Presence of Biofouling on Marine/Offshore Structures, a Review and New Approach. *J. Mar. Sci. Eng.* **2022**, *10*, 558. [CrossRef]
6. Tuck, B.; Watkin, E.; Somers, A.; Machuca, L.L. A critical review of marine biofilms on metallic materials. *npj Mater. Degrad.* **2022**, *6*, 25. [CrossRef]
7. Davidson, I.; Cahill, P.; Hinz, A.; Kluza, D.; Scianni, C.; Georgiades, E. A Review of Biofouling of Ships' Internal Seawater Systems. *Front. Mar. Sci.* **2021**, *8*, 761531. [CrossRef]
8. Liu, Z.; Zheng, X.; Zhang, H.; Li, W.; Jiang, R.; Zhou, X. Review on formation of biofouling in the marine environment and functionalization of new marine antifouling coatings. *J. Mater. Sci.* **2022**, *57*, 18221–18242. [CrossRef]
9. Jiao, S.; Zhang, X.; Sun, L.; Shi, Y.; Zhang, M. Structural Design and Horizontal Wave Force Estimation of a Wall-Climbing Robot for the Underwater Cleaning of Jackets. *J. Mar. Sci. Eng.* **2024**, *12*, 1612. [CrossRef]
10. Luo, G.; Luo, C.; Gao, S.; Xu, J.; Bao, X.; Ma, Z.; Jiang, Z. Research on passive adaptive wall-climbing cleaning and inspection robot of marine cylindrical steel structure based on conical magnetic adsorption wheel. *Ocean Eng.* **2024**, *314*, 119676. [CrossRef]

11. Chen, L.; Cui, R.; Yan, W.; Xu, H.; Zhao, H.; Li, H. Design and climbing control of an underwater robot for ship hull cleaning. *Ocean Eng.* **2023**, *274*, 114024. [CrossRef]
12. Wang, B.; Ni, Z.; Shen, Y.; Zhang, S.; Shen, Q.; Niu, X.W. Design and analysis of a wheel-leg compound variable curvature ship hull cleaning robot. *Ocean Eng.* **2022**, *266*, 112755. [CrossRef]
13. Jiang, Z.; Zhao, Z.; Chen, B.; Li, Y.; Zhao, Y.; Xu, Y. Design and analysis of a passive adaptive wall-climbing robot based on five-bar mechanisms. *Ocean Eng.* **2024**, *298*, 117140. [CrossRef]
14. Wei, K.; Zhang, Z.; Zhou, Z. Design of a new composite underwater hull cleaning robot. *J. Sea Res.* **2024**, *198*, 102488. [CrossRef]
15. Zhong, X.; Dong, J.; Liu, M.; Meng, R.; Li, S.; Pan, X. Experimental study on ship fouling cleaning by ultrasonic-enhanced submerged cavitation jet: A preliminary study. *Ocean Eng.* **2022**, *258*, 111844. [CrossRef]
16. Zhu, H.; Pan, S.; Zhang, X.; Zhu, R.; Xie, Z. Cavitation-induced cleaning characteristics of barnacle fouling on hull surfaces using high-speed water jets. *Ocean Eng.* **2025**, *340*, 122466. [CrossRef]
17. Zhang, M.; Sun, L.; Xu, W.; Yao, Y.; Zhang, X. Numerical Investigation into Hydrodynamic Interactions Between an Open-Frame Underwater Cleaning Robot and a Full-Scale Floating Production Storage and Offloading. *J. Shanghai Jiaotong Univ. (Sci.)* **2024**, *31*, 405–419. [CrossRef]
18. Zhang, X.; Huo, J.; Zhang, M.; Cai, X.; Wang, B.; Xie, Z. Maneuverability characteristics of a fouling submarine near the seabed. *Ocean Eng.* **2025**, *315*, 119773. [CrossRef]
19. Fang, Z.; Ji, Z.; Kang, D.; Chen, Y.; Zhang, X.; Wang, S.; Xiong, T. Cavitation damage characteristics following marine fouling cleaning by a self-excited oscillation cavitation waterjet. *Appl. Ocean Res.* **2023**, *139*, 103692. [CrossRef]
20. Puc, U.; Abina, A.; Salvi, E.; Malačič, V.; Francé, J.; Zanelli, R.; Zidanšek, A. Development and Field Testing of a Cavitation-Based Robotic Platform for Sustainable In-Water Hull Cleaning. *J. Mar. Sci. Eng.* **2026**, *14*, 227. [CrossRef]
21. SNAME. *Nomenclature for Treating the Motion of a Submerged Body Through a Fluid*; The Society of Naval Architects and Marine Engineers: New York, NY, USA, 1950.
22. Fossen, T.I. *Guidance and Control of Ocean Vehicles*; Wiley: Chichester, UK; New York, NY, USA, 1994.
23. Shi, S.D. *Submarine Maneuverability*; National Defense Industry Press: Beijing, China, 1995.
24. Xue, G.; Bai, F.; Guo, L.; Ren, P.; Liu, Y. Research on the effects of complex terrain on the hydrodynamic performance of a deep-sea fishlike exploring and sampling robot moving near the sea bottom. *Front. Mar. Sci.* **2023**, *10*, 1091523. [CrossRef]
25. Zhang, L.; Shi, W.; Zeng, Y.; Michailides, C.; Zheng, S.; Li, Y. Experimental investigation on the hydrodynamic effects of heave plates used in floating offshore wind turbines. *Ocean Eng.* **2023**, *267*, 113103. [CrossRef]
26. Hang, L.C.; Rosli, N.A.N.; Wahid, M.A.; Othman, N.; Mat, S.; Zain, M.Z.M. CFD Analysis on Propeller at Varying Propeller Disc Angle and Advance Ratio. *J. Adv. Res. Fluid Mech. Therm. Sci.* **2022**, *96*, 82–95. [CrossRef]

Disclaimer/Publisher's Note: The statements, opinions and data contained in all publications are solely those of the individual author(s) and contributor(s) and not of MDPI and/or the editor(s). MDPI and/or the editor(s) disclaim responsibility for any injury to people or property resulting from any ideas, methods, instructions or products referred to in the content.